



# Effect of freeform surfaces on the volume and performance of unobscured three mirror imagers in comparison with off-axis rotationally symmetric polynomials

ERIC M. SCHIESSER,\* AARON BAUER, AND JANNICK P. ROLLAND

*Institute of Optics, University of Rochester, 275 Hutchison Road, Rochester, NY 14627, USA*

*\*eric.schiesser@rochester.edu*

**Abstract:** The invention of new design techniques for unobscured reflective systems using freeform surfaces has expanded the optical design space for these system types. We illustrate how the use of freeform surfaces can expand the design space of the Three Mirror Compact design type to allow both better performance at a given system volume and smaller volumes for a given performance target. By evolving designs using conventional off-axis asphere type surfaces to ever smaller volumes and then converting these off-axis asphere descriptions to centered Zernike descriptions, we show that the wavefront error improves by up to 69% in this case by allowing the surfaces to break rotational symmetry. In addition, we show that evolving designs from the same starting point as the off-axis asphere designs but instead using a centered Zernike description can produce a design with a 39% smaller volume in this case while maintaining the same diffraction-limited performance.

© 2019 Optical Society of America under the terms of the [OSA Open Access Publishing Agreement](#)

## 1. Introduction

One of the advantages often ascribed to freeform optical surfaces is their ability to reduce the mass or volume of rotationally non-symmetric optical systems while maintaining (and in some cases, exceeding) optical performance [1–4]. To investigate this volume reduction capability of freeform surfaces, we focus on the design of unobscured three mirror imagers. There are many traditional forms of such optical systems, including the three-mirror anastigmat (TMA) and the reflective triplet. Also known as the three-mirror compact (TMC), the unobscured reflective triplet is often touted as the most compact (in terms of overall length and volume) form of unobscured three mirror imager design [5–7]. The TMC and TMA have been popular design forms for improvement using freeform surfaces [4,8–10].

The present work compares the effectiveness of two surface types in reducing the volume of unobscured TMC designs. One is a traditional surface type, the off-axis section of a rotationally symmetric aspheric parent. The second surface type is a field-centered FRINGE Zernike freeform surface. We will use the FRINGE ordering of terms as specified in the CODE V manual throughout this work, so “FRINGE Zernike” will be shortened to simply “Zernike” or interchangeably “freeform” throughout [11]. We used Zernike polynomial surfaces in this study for a number of reasons. First, they are a complete polynomial set and they are orthogonal. Second, they are the basis set used in the aberration theory of freeform surfaces (ATFS) [12]. Additionally, Zernikes are well understood, simple to implement, and typically provide the required degrees of freedom according to the ATFS. Prior work has shown that Zernikes are equally capable for freeform design as other orthogonal polynomials [13], and there are many examples of effective reflective systems using Zernike polynomial surface descriptions [2,12,14,15].

The designs using sections of rotationally symmetric parent surfaces will be referred to as three-mirror compact asphere (TMCA) designs and the designs using Zernike surfaces will be referred to as three-mirror compact freeform (TMCF) designs in this work.

In systems using off-axis sections of rotationally symmetric surfaces, field-bias and aperture offset are used to unobscure the system. The field bias and aperture offset are akin to a tilt and/or decenter of the surface with respect to the local object and image and the local entrance and exit pupils for that surface. Because the field bias and aperture offset remove any rotational symmetry in the field-dependence of the aberrations, the parent surfaces of the TMCA designs should not be restricted to sharing an axis of rotational symmetry, as this restriction would impose an added constraint on the TMCA designs not present in the TMCF designs. This is analogous to the TMCF, which uses tilted surfaces to avoid obscuration rather than field-bias and aperture offset. Thus, the only difference from an aberration standpoint between a non-coaxial TMCA and a TMCF are the restrictions on the surface shape that can be used to correct the optical aberrations. Freeform surfaces allow more degrees of freedom than rotationally symmetric surfaces do because their aberration contributions can be decoupled from each other, as shown by Fuerschbach et al. [16].

The basic thesis of this work is that non-coaxial TMCA have fewer layout options than TMCFs. The way we exemplify this property is by starting with plane-symmetric, unobscured non-coaxial TMCA designs from the literature and showing that, by adding freeform terms to the surfaces, more plane-symmetric aberrations can be corrected; thus, allowing more layout options for a given performance level, or better performance for a given first-order layout.

First, we describe the design process for the TMCA and a process to progressively reduce the volume target. Next, we show that these TMCA designs can be converted to TMCF designs with the same surface shapes but described using centered Zernike polynomials, which we term the TMCF Converted designs. We then show that, without changing the first-order layout, the Zernike polynomials can further correct aberrations that were not possible with the off-axis asphere descriptions of the TMCA. These designs will be termed TMCF Frozen-Geometry designs. Next, we use the same volume reduction algorithm on the TMCF designs to progressively reduce the volume to determine the volume-performance relationship for comparison to the TMCA-based designs. These designs are termed TMCF Volume-Optimized designs. Finally, we summarize and discuss the results by looking at the aberration full-field displays (FFDs) and the surface departures. For readability, the acronyms and descriptions for each design completed in this work are summarized in Table 1.

**Table 1. Naming convention and descriptions for the designs completed in this work**

Design Name	TMCA	TMCF Converted	TMCF Frozen-Geometry	TMCF Volume-Optimized
Surface Type	Off-axis $Q_{CON}$	Centered Fringe Zernike	Centered Fringe Zernike	Centered Fringe Zernike
Description	Off-axis asphere designs, optimized for a given volume from 110 L to 70 L	Off-axis asphere designs converted to centered Zernike surface types (Identical in performance and first-order layout to TMCA designs)	TMCF Converted designs whose surface shapes are optimized for aberration correction	TMCF designs optimized for a given volume from 110 L to 50 L
Layout optimized for a given volume?	Yes	No	No	Yes
Surface coefficients optimized?	Yes	No	Yes	Yes

## 2. Traditional TMC design – the TMCA

The TMC uses a positive-negative-positive power distribution without an internal image, similar to the (refractive) Cooke triplet. Traditionally, TMCs are effective with the aperture

stop at the primary or at the secondary [7], both having certain advantages depending on the use case. The aperture stop at the secondary is best for controlling aberrations (similar to the Cooke triplet) and allows for telecentricity in image space if needed. This work will focus on TMC configurations with the aperture stop at the secondary.

Traditional design techniques for unobscured three mirror imagers using rotationally symmetric surfaces typically start with a co-axial, rotationally symmetric, third-order aberration corrected design, which can be obtained using myriad methods [17–19]. These co-axial designs then use field-bias or aperture offset to remove the obscuration. Many designs restrict the parent surfaces to remain co-axial, while others allow the parent surfaces to tilt and decenter relative to one another after they are unobscured. Other approaches do not start from rotationally symmetric designs, but instead consider tilted components with rotationally symmetric parent surfaces (usually beginning with off-axis conics) [20–24]. These techniques may start with given airspaces and radii, but do not allow specification of volume as a parameter to constrain the solution. One difficulty with specifying the volume as a constraint on the first- or third-order solution from these techniques is that there may be many first- or third-order layouts that lead to a given volume from these techniques. In this study, since we are primarily concerned with the relationship between volume and performance, we started from a well-corrected non-coaxial TMCA design example and evolved it to meet our performance goals. The alternative would have been to create a new first- or third-order starting point at each volume target.

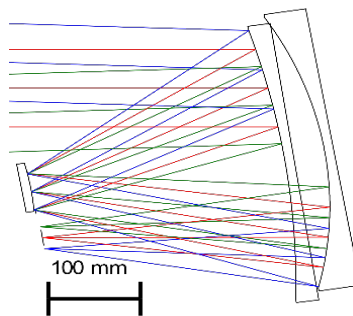


Fig. 1. The layout of the *threemrc.len* example lens in CODE V, a TMCA type design.

The reference design is the *threemrc.len* file included with the CODE V optical design software shown in Fig. 1. The reference design uses a conic primary, a conic secondary, and a 10th order aspheric tertiary. This design was adapted to first fit the system specifications used in this work, as reported in Table 2. Specifically, the system was scaled up by 2.5x to increase the entrance pupil diameter (EPD) from 100 mm to 250 mm. Next, all three surfaces were converted to  $Q_{CON}$  surface types, which allow up to 30th radial order aspheric surface sag to be added to a base conic [25]. Using aspheres with higher-order polynomial terms allows for more aberration correction when the design is re-configured for a smaller volume than a simple conic surface might allow.  $Q_{CON}$  surfaces are normalized and orthogonal, which helps with convergence, as shown by Forbes [25].

Table 2. System specifications for the TMCA and TMCF designs

Parameter	TMCA Specification	TMCF Specification
Entrance pupil diameter (mm)	250	Same
F-Number	F/3.0	Same
Number of mirrors	3	Same
Distortion	< 5%	Same
Square field-of-view (degrees)	3.75 x 3.75	Same
Surface type	Off-axis $Q_{CON}$	Centered FRINGE Zernike
Wavelength for evaluation (nm)	587	Same
Volume (L)	110 to 70	110 to 50

To reduce the volume, the airspaces and radii were allowed to vary so that a volume reduction constraint could be applied. The  $Q_{CON}$  surface terms up to 22nd order were allowed to vary. In preliminary studies, terms higher than 22nd order did not have a beneficial effect on aberration correction and tended to slow down the optimization. The surface y-decenters and tilts about the x-axis were also allowed to vary. It was important to vary the surface decenters as it allowed different portions of the aspheric surface to be used for aberration control and was key to volume minimization. Clearance constraints were used to maintain the unobscured form. To maintain clearance, the clear-aperture of each surface is constrained to be greater than 5 mm from the closest ray.

The volume was determined by a simple algorithm calculating the smallest rectangular box that bounds all the surface-ray intersections. The surface-ray intersections were calculated in global coordinates relative to a given surface's coordinate axes orientation. To compute the volume of the bounding box, the maximum and minimum coordinate along each (x,y,z) axis is computed and the difference is taken to give an extent along each axis ( $L_x$ ,  $L_y$ ,  $L_z$ ). The volume of the bounding box is then the product of the lengths. To find the minimum bounding box, this procedure is repeated while rotating the coordinate frame, as illustrated in Fig. 2, and the minimum volume is taken to give the smallest bounding rectangular box's volume. This was repeated relative to each surface and the smallest volume was chosen. This simple volume algorithm allows us to quickly compute the volume and constrain the layout to The full Zernike coefficients are listed given volume target. It is important to note, however, that this volume may not be the as-built volume, for which other parameters must be considered, such as the thickness of the mirror substrates, the mirror mounting hardware, the detector housing size, etc. Even so, the optical ray-based volume we are using in this study and the as-built volume that considers these parameters are likely closely related by a multiplicative factor, *ceteris paribus*.

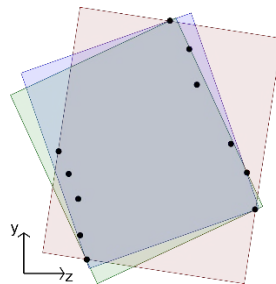


Fig. 2. Diagram of surface-ray intersection coordinates (black dots) in the Y-Z plane at  $x = 0$  and three bounding boxes in different coordinate frames (red, blue and green).

By using this volume algorithm as a constraint in optimization, the radii and airspaces were able to change to fit the volume target. The volume was optimized to reduce the volume to a target of 100 L, which was chosen based on previous studies to achieve a compact, diffraction-limited design. To ascertain the performance at increasingly smaller volumes, the volume

constraint target was progressively reduced in 0.1 L increments from 100 L down to 70 L to obtain TMCA designs of varying performance and volume. The volume target was also increased from 100 L up to 110 L, using the same procedure, to see the trend. This iterative approach allowed the surface coefficients to re-optimize for each slightly smaller volume. At each volume increment, first STEP optimization was used and then damped least squares optimization was used in succession to minimize the wavefront error while maintaining the volume target (see Chapter 3 in the CODE V Optimization Reference Manual [26]). One advantage of this optimization approach is that it is able to find well-optimized designs for a given volume for both TMCA and TMCf type designs by using small volume increments and taking advantage of standard optimization routines in CODE V. One disadvantage is that this process is lengthy due to the small volume increments. It is possible that local minima are found (as with any complex optical design problem) but using STEP optimization and small increments help to avoid local minima.

The resulting wavefront error (WFE) performance ranges from a field-averaged  $0.062 \lambda$  RMS WFE at 110 L up to  $0.31 \lambda$  RMS WFE at 70 L. The full volume data are shown in Fig. 3. The smallest volume for which the TMCA design has average RMS WFE at or below the diffraction limit (i.e.  $0.07 \lambda$ ) is 96.9 L.

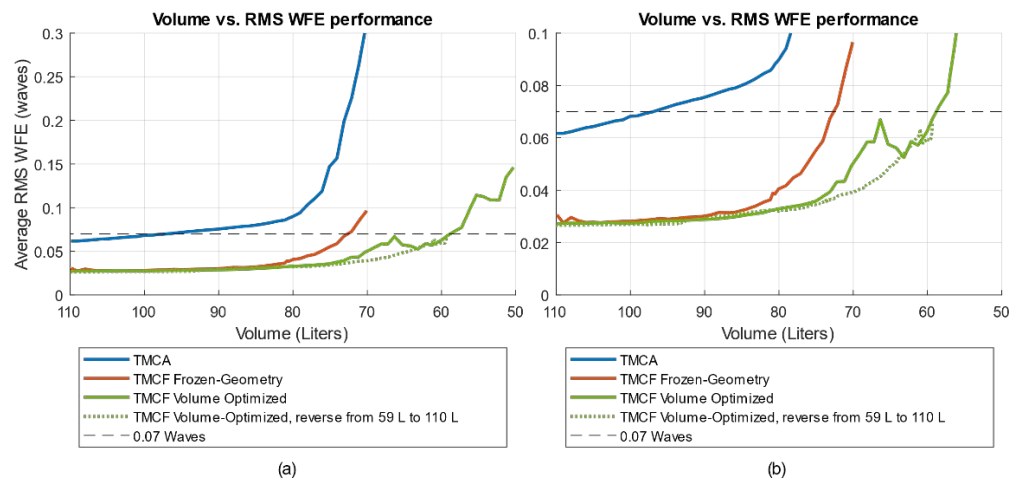


Fig. 3. (a) Field-averaged RMS WFE performance versus volume for each design type. The original TMCA design optimized for volume (blue line) crosses the 0.07 waves line at 96.9 L. The TMCf Frozen-Geometry design (red line) crosses the 0.07 waves line at 72.6 L. The TMCf Volume-Optimized design (yellow line) crosses the 0.07 wave line at 59.0 L. The reverse optimization from 59 L to 110 L of the TMCf Volume-Optimized design (dashed green line) avoids the local minimum of the TMCf Volume-Optimized forward optimization. (b) The same data as the chart in (a), showing more detail in the 0.0 to 0.1 waves range.

### 3. Conversion of TMCA designs to centered Zernike surfaces

To determine the amount of improvement afforded by freeform surfaces for a given first-order geometry, each TMCA design was converted from the off-axis asphere geometry to the centered Zernike geometry. An algorithm was devised and implemented in a CODE V script to convert the TMCA designs to the equivalent centered Zernike designs. The algorithm captures a 3D surface profile of the effective aperture of each surface to produce a point cloud and the coordinates are transformed such that the chief ray of the central field point defines the origin of each surface. The coordinates are then tilted about the local x-axis such that the surface normal is perpendicular to the local X-Y plane. This configuration is conducive to using a decenter-and-bend (BEN) surface type in CODE V because there will be zero tilt at the center of the surface, and as such the tilt about the x-axis (alpha tilt in CODE V) is equal to the angle of incidence of the optical axis ray. The point cloud data for each surface is then fitted with a

best fit sphere (BFS), and the residual sag after subtraction of the BFS is fitted with Zernike terms up to Z37. For each TMCA design, the decenter-and-return (DAR) surface decenters are converted to centered decenter-and-bend (BEN) surface decenters with only a tilt about the x-axis. The surfaces are converted to Zernike FRINGE (ZFR) surface types and the computed coefficients are entered. The RMS WFE of the converted designs differ by less than 1% from 110 L to 80 L, by less than 3.5% from 80 L to 70 L, and by 0.7% on average to the original TMCA designs. These designs, referred to as “TMCF Converted” designs, as reported in Table 1, each have the same first-order geometry as the TMCA designs of the same volume, but are simply represented by centered Zernike surface types instead of off-axis aspheres.

#### 4. Additional WFE correction for the TMCF Converted designs using freeform surfaces

To determine the amount of improvement afforded by freeform surfaces, the surface shapes of the TMCF Converted designs were optimized. Specifically, the Y-Z plane symmetric surface terms up to Z25 were allowed to vary. In these designs, referred to as TMCF Frozen-Geometry as reported in Table 1, the first-order geometry, as their name indicate, was kept frozen (airspaces, radii, and surface tilt angles) to facilitate a comparison to the originating TMCA design of the same volume.

As seen in Fig. 3, the TMCF Frozen-Geometry designs significantly improved upon the average RMS WFE of the designs.

The improvement in RMS WFE compared to the TMCA designs at each volume ranges from 0.031 waves at a volume of 110 L (a 50.4% improvement) up to 0.22 waves at a volume of 70 L (a 69.2% improvement). The average percent RMS WFE improvement over the range of volumes from 110 L to 70 L is 57.4%.

This analysis shows that, for a TMCA geometry optimized for a given volume, the performance can typically be significantly improved by allowing the surface to depart from rotational symmetry by adding freeform terms to the surface. Said another way, the optimal surfaces for an unobscured TMC with a given volume are not, in general, sections of surfaces with rotationally symmetric parents.

#### 5. Additional volume reduction using freeform surfaces

We have seen that a given TMCA first-order layout can achieve a lower RMS WFE by allowing the surfaces to break rotational symmetry. However, for a given volume target, we hypothesize that the optimal TMCF first-order geometry may be different than the optimal TMCA layout, since the freeform surfaces of the TMCF can better correct the plane-symmetric aberrations. To test this hypothesis, we used the same volume reduction algorithm as the TMCA designs to create TMCF designs for each volume, starting with the 110 L TMCF Frozen-Geometry, and progressively reducing the volume target down to 50 L.

Like the TMCA volume reduction, the TMCF airspaces and radii were allowed to vary. The plane-symmetric Zernike terms up to Z25 (12 terms in total) were also allowed to vary. The magnitude of the Zernike power term and the magnitude of the linear tilt terms were constrained such that there is no Zernike power, tilt, or piston at the center of the surface. The resulting volume vs. average RMS WFE performance is shown in Fig. 3. The resulting design with the smallest volume having an average RMS WFE close to 0.07 waves has a volume of 59 L, a 39% reduction in volume compared to the diffraction-limited TMCA design.

In addition to the volume reduction curve for the TMCF Volume-Optimized designs shown in Fig. 3, the optimization procedure was repeated in reverse starting from 59 L up to 110 L. As we can see, this reverse optimization produces a smoothly varying line from 80 L down to 65 L and avoids the local minimum in the forward curve.



## 6. Discussion

The above results illustrate that rotationally symmetric surfaces do not typically produce the optimal surface shapes for a given first-order geometry when used in the context of a system that inherently lacks rotational symmetry such as the unobscured TMC design form. To understand why this is the case, we compare the three design types, TMCA, TMCF Frozen-Geometry, and TMCF Volume-Optimized across similar volumes (iso-volume) and across similar performance levels (iso-performance).

### 6.1 Iso-volume comparison

It is instructive to compare the three designs types at the same volume. A volume of 72.5 L is the volume at which the TMCF Frozen-Geometry design is just below 0.07 waves average RMS WFE. At this volume, Fig. 4 shows the layouts for each of the three design types. The layouts for both the TMCA and the TMCF Frozen-Geometry designs are different from the TMCF Volume-Optimized design. The centered Zernike surfaces are able to correct plane-symmetric aberrations according to the ATFS [12], and therefore, the TMCF Volume-Optimized design can take advantage of a first-order geometry that the TMCA cannot adequately correct, and therefore achieves a lower RMS WFE. The optimal first-order layout when using freeform surfaces is different than the optimal layout using rotationally symmetric surfaces, as seen by comparing the two layouts in Fig. 4(a) and 4(b) with the layout in Fig. 4(c).

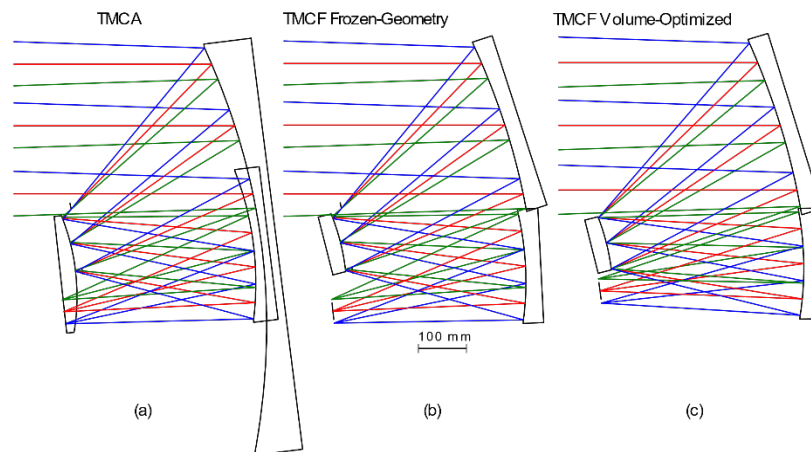


Fig. 4. Layouts of each design type corresponding to a volume of 72.5 L, the smallest diffraction-limited volume of the TMCF Frozen-Geometry: (a) The TMCA, (b) TMCF Frozen-Geometry, and (c) the TMCF Volume-Optimized designs. Note that the apparent overlap of the surfaces in the layouts is due to the extension of the surfaces in the drawing program. The clear apertures and the rays have no conflicts in the designs.

The level and type of aberration correction can be seen by examining the full-field displays (FFD) of the Zernike aberrations for each of these designs. An FFD represents the magnitude and, where appropriate, orientation of a given aberration across the full field-of-view using a symbol. In general, comparing the TMCA and TMCF Frozen-Geometry designs, we see that the TMCF Frozen-Geometry design is better able to correct the plane-symmetric aberrations, or when correction is not possible (or not optimal), to achieve a better balance of the field-dependence. For example, Fig. 5 shows the Zernike defocus FFD. The TMCA design has some higher-order field curvature, while the TMCF Frozen-Geometry design is able to substantially correct this aberration through balancing with a combination of Z4, Z8, Z9, Z12, and Z15 Zernike surface coefficients. Figure 6 shows that the astigmatism is substantially reduced in both TMCF designs, with two astigmatism nodes being brought into the FOV. The same is true for coma in Fig. 7 and spherical in Fig. 8. Furthermore, the TMCF Volume-Optimized design

is able to achieve a better balance of these aberrations by changing the first-order layout. Additionally, the TMCF designs are able to directly correct the field-constant elliptical coma present in the TMCA design as seen in Fig. 9.

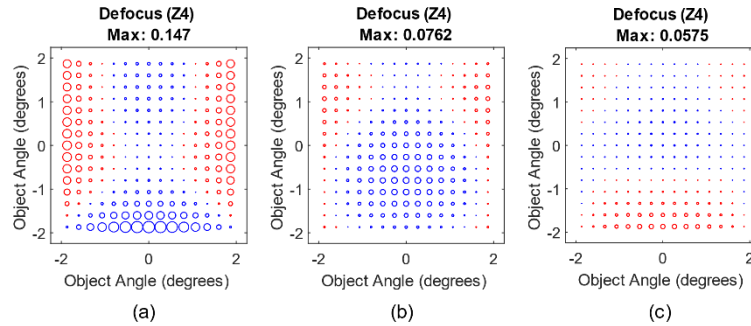


Fig. 5. Zernike defocus ( $Z_4$ ) FFD for the (a) TMCA design, (b) TMCF Frozen-Geometry design, and (c) TMCF Volume-Optimized design. Blue indicates a positive value, red indicates a negative value.

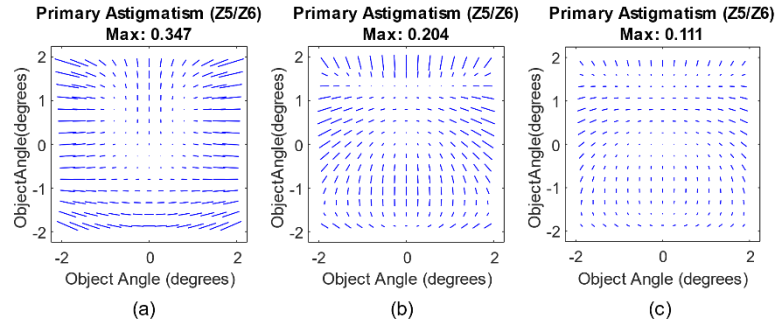


Fig. 6. Zernike Astigmatism ( $Z_5/Z_6$ ) FFD for the (a) TMCA design, (b) TMCF Frozen-Geometry design, and (c) TMCF Volume-Optimized design.

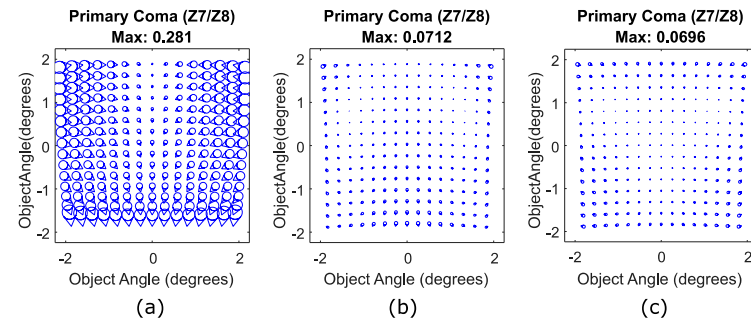


Fig. 7. Zernike coma ( $Z_7/Z_8$ ) FFD for the (a) TMCA design, (b) TMCF Frozen-Geometry design, and (c) TMCF Volume-Optimized design.



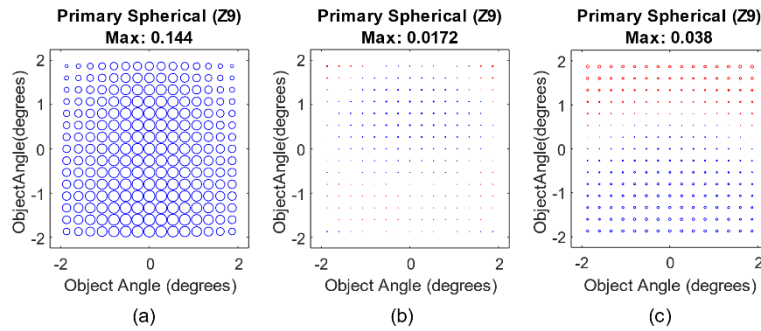


Fig. 8. Zernike spherical aberration (Z9) FFD for the (a) TMCA design, (b) TMCF Frozen-Geometry design, and (c) TMCF Volume-Optimized design. Blue indicates a positive value, red indicates a negative value.

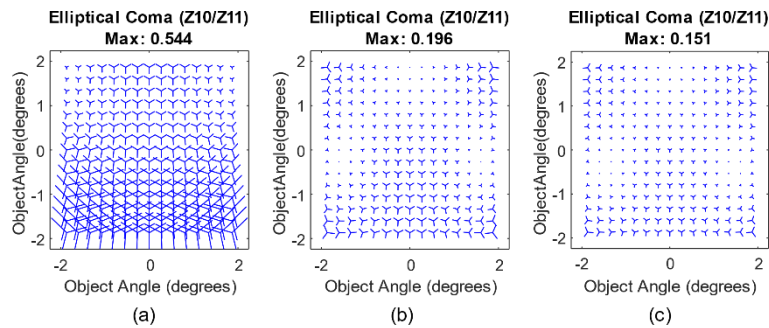


Fig. 9. Zernike elliptical coma (Z10/Z11) FFD for the (a) TMCA design, (b) TMCF Frozen-Geometry design, and (c) TMCF Volume-Optimized design.

Not only do the freeform surfaces allow for better correction of the rotationally non-symmetric aberrations, but they also allow for better correction of rotationally symmetric aberrations because of their beam-centered coordinate reference. Since the Zernike surface departure is centered on the surface, the rotationally symmetric Zernike terms (Z4, Z9, Z16, Z25) can contribute directly to the correction of rotationally symmetric aberration terms, in contrast to the off-axis asphere sections, where the rotationally symmetric contributions are not separable from the plane-symmetric contributions. Similarly, the plane-symmetric terms can contribute directly to the correction of plane-symmetric aberrations as determined by the ATFS [12]. For example, Fig. 8 shows the Zernike spherical aberration for which there is a substantial uncorrected field-constant term, but this can be removed directly using a Z9 surface shape at the stop surface (or any other surface, for that matter [2,12]).

As seen in Table 3, the surface shapes in the TMCF designs depart further from a base sphere in general. Except for M1 of the TMCA, the freeform surfaces depart more than the off-axis aspheres. This extra departure is directly related to the centered nature of the Zernike surfaces. When using off-axis aspheres, the surface coefficients are not orthogonal and are furthermore coupled together in terms of their aberration correction abilities. However, the centered Zernike surface terms are able to independently add surface departure and aberration correction, and thus achieve better correction, while adding more departure. This is the inherent tradeoff in achieving better correction through freeform surfaces, though recent work has shown that the effect can be reduced by constraining the surface coefficient magnitudes without sacrificing much correction ability [13].

Table 3. Departure from Base Sphere for each design type in the iso-volume comparison

	Maximum Departure from Base Sphere (microns)		
	TMCA	TMCF Frozen-Geometry	TMCF Volume-Optimized
M1	370	283	251
M2	20	172	239
M3	12	264	175

## 7. Iso-performance comparison

Another illustrative comparison is between TMC designs of the same performance. The layouts of the three designs closest to 0.07 waves RMS WFE for each design type are shown in Fig. 10. The volumes of each bounding box are 96.9 L, 72.5 L, and 59.1 L in Figs. 10(a), 10(b), and 10(c), respectively. The bounding boxes are also shown overlaid in Fig. 10(d).

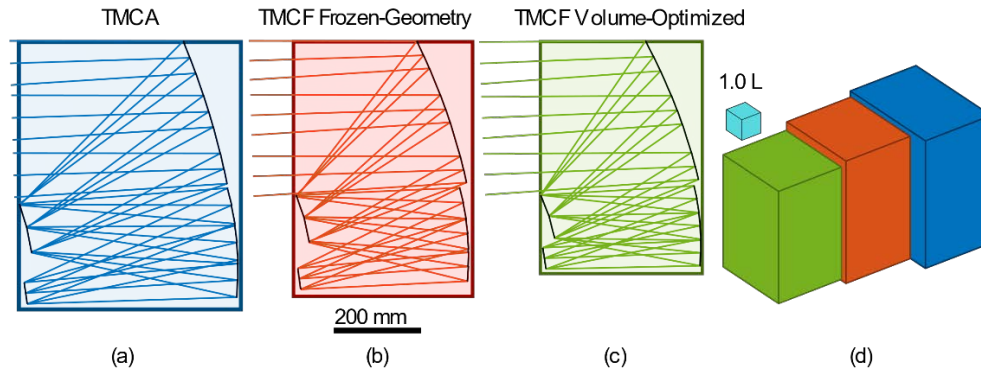


Fig. 10. Layouts of the smallest volume diffraction-limited designs of each TMC type with their bounding boxes: (a) The TMCA is shown with a blue bounding box, (b) the TMCF Frozen-Geometry is shown with a red bounding box, and (c) the TMCF Volume-Optimized is shown with a green bounding box. (d) The bounding boxes are shown next to each other for perspective.

The FFDs for each design type are shown in Figs. 11-13. Though these designs share similar overall RMS WFE performance, they achieve a different balance of aberrations, similar to the iso-volume comparison in Section 6a. Notably, the coma and higher order field-curvature are substantially reduced in both TMCF designs, while the plane-symmetric astigmatism terms actually increase for the TMCF designs. Evidently, the balance of aberrations in the TMCF designs allows the first-order layout to shift to a lower volume configuration.

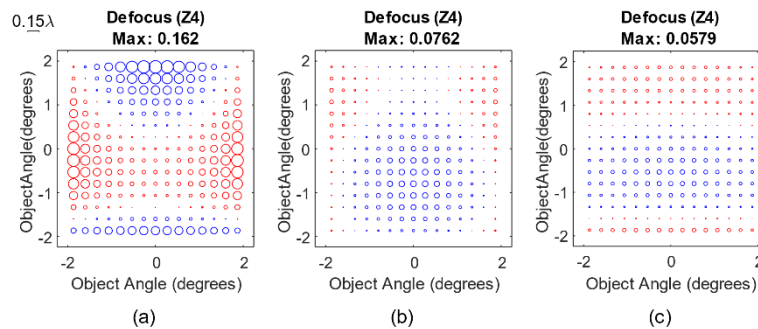


Fig. 11. Zernike defocus (Z4) FFD for the: (a) TMCA design, (b) TMCF Frozen-Geometry design, and (c) TMCF Volume-Optimized design. Blue indicates a positive value, red indicates a negative value.

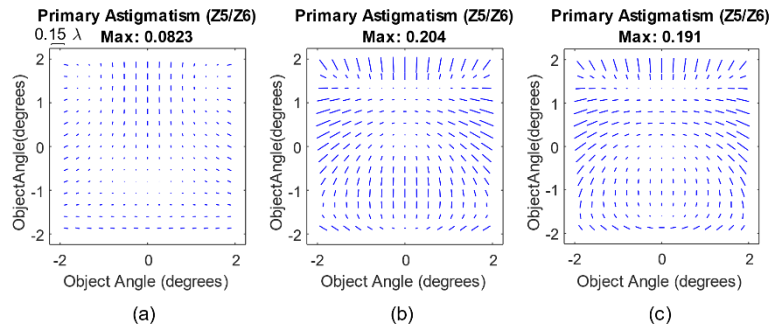


Fig. 12. Zernike Astigmatism (Z5/Z6) FFD for the: (a) TMCA design, (b) TMCF Frozen-Geometry design, and (c) TMCF Volume-Optimized design.

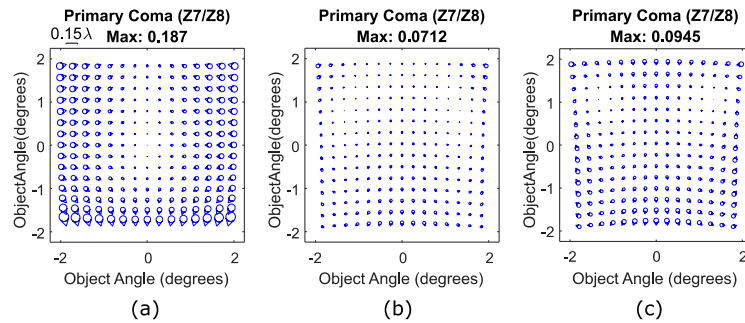


Fig. 13. Zernike coma (Z7/Z8) FFD for the: (a) TMCA design, (b) TMCF Frozen-Geometry design, and (c) TMCF Volume-Optimized design.

Table 4 shows the departure from base sphere for each design type for the iso-performance case. We are showing the surface departure as a way of comparing the aspheric nature of each surface. For surfaces with slowly varying shapes like the low-order Zernike polynomials used in this article, the sag and slope are closely correlated, so we have shown the maximum sag departure from base sphere. The TMCA design has substantially lower departure than either TMCF designs due largely to its larger volume and therefore slower surfaces. The surface departures of the primaries in all geometries contribute most of the departure, but the departure in both TMCF geometries are more balanced, and thus the aberration correction happening at each surface is more balanced as well. This trade-off in volume vs departure is not inherent to freeform, but it is accentuated by it. Faster optical surfaces are required for smaller volumes, and tilting those faster optical surfaces creates more off-axis aberrations, resulting in more required departure to correct those aberrations. However, freeform surfaces have more degrees of freedom, allowing for more modes of departure, and therefore can achieve the larger departures required to maintain performance at a given volume compared to off-axis sections of rotationally symmetric parent surfaces. The full Zernike coefficients are listed in Tables 5-7 in the Appendix for reference.

**Table 4. Departure from base sphere for each design type in the iso-performance comparison**

	TMCA	TMCF Frozen- Geometry	TMCF Volume- Optimized
Mirror	Maximum departure from base sphere (microns)		
M1	208	310	488
M2	14	177	205
M3	20	204	169

## 8. Conclusion

The ability of freeform surfaces to expand the design space for plane-symmetric unobscured optical systems allows better overall correction of plane-symmetric aberrations for a given volume resulting in greater performance for a given volume. This has been demonstrated by progressively reducing the volume of a TMC design that uses rotationally symmetric surfaces and converting the layout to an equivalent field-centered freeform design that is shown to better correct the aberrations. Additionally, freeform surfaces allow for more compact first-order layouts, which are not otherwise correctable using rotationally symmetric surfaces. This was demonstrated by allowing the first-order layout of the converted designs to vary and achieving not only better correction by up to 70%, but smaller volume as well by up to 39%. Finally, a reduced volume comes at the expense of more freeform departures from the base sphere by up to an order of magnitude.

## Appendix

**Table 5. The FRINGE Zernike coefficients for the primary mirror representing departure from base sphere for each diffraction-limited design.**

	TMCA 96.9 L	TMCF Frozen-Geometry 72.5 L	TMCF Volume-Optimized 59.1 L
Maximum Aperture Semi-Diameter (mm)			
	176.3330	176.3297	178.3835
Normalization Aperture Semi-Diameter (mm)			
	170.7363	176.3297	178.3835
FRINGE Zernike Coefficient, Primary Mirror (mm)			
Z1	0.0002458149	-0.0499511345	-0.0459181158
Z2	0	0	0
Z3	0.1165349914	0.2743568100	0.3637282551
Z4	0.0000693106	-0.0745891417	-0.0686044094
Z5	-0.1353639608	-0.1303619649	-0.3191715585
Z6	0	0	0
Z7	0	0	0
Z8	0.0580866222	0.1368588872	0.1813839316
Z9	0.0042482223	-0.0244205099	-0.0225119102
Z10	0	0	0
Z11	0.0021226646	-0.0111876327	-0.0053145466
Z12	0.0008326605	0.0032969007	0.0044426267
Z13	0	0	0
Z14	0	0	0
Z15	-0.0001083608	-0.0002331794	-0.0003350693
Z16	0.0000027475	0.0002118401	0.0001687888
Z17	0.0000613417	-0.0000150526	0.0000036374
Z18	0	0	0
Z19	0	0	0
Z20	-0.0000238739	-0.0001049851	-0.0001578434
Z21	-0.0000058420	-0.0000020773	-0.0000120510
Z22	0	0	0
Z23	0	0	0
Z24	0.0000014837	-0.0000151256	-0.0000112040
Z25	-0.0000009877	-0.0000056571	-0.0000055946
Z26	0	0	0
Z27	-0.0000051085	0	0
Z28	-0.0000011038	0	0
Z29	0	0	0
Z30	0	0	0
Z31	-0.0000002160	0	0
Z32	0.0000004731	0	0
Z33	0	0	0
Z34	0	0	0
Z35	-0.0000007115	0	0
Z36	-0.0000008351	0	0
Z37	-0.0000003518	0	0

**Table 6. The FRINGE Zernike coefficients for the secondary mirror representing departure from base sphere for each diffraction-limited design.**

	TMCA 96.9 L	TMCF Frozen-Geometry 72.5 L	TMCF Volume-Optimized 59.1 L
Maximum Aperture Semi-Diameter (mm)			
	58.8430	58.1558	51.8783
Normalization Aperture Semi-Diameter (mm)			
	59.8540	58.1558	51.8783
FRINGE Zernike Coefficient, Secondary Mirror (mm)			
Z1	-0.0000370732	0.0040222707	-0.0432379214
Z2	0	0	0
Z3	-0.0108838775	0.0309447052	0.0519336946
Z4	-0.0000594983	0.0060388280	-0.0641484832
Z5	0.0075685216	0.1637450199	0.0459991873
Z6	0	0	0
Z7	0	0	0
Z8	-0.0056694096	0.0152122037	0.0258454803
Z9	-0.0009023299	0.0020221364	-0.0204517791
Z10	0	0	0
Z11	0.0004316819	-0.0129031757	-0.0079094718
Z12	0.0003507853	0.0014483055	0.0008160642
Z13	0	0	0
Z14	0	0	0
Z15	-0.0001534008	-0.0001660436	-0.0000823412
Z16	-0.0000141538	0.0000070524	0.0004486702
Z17	0.0000094924	-0.0001867808	-0.0001358152
Z18	0	0	0
Z19	0	0	0
Z20	-0.0000069325	-0.0000450512	-0.0000314659
Z21	-0.0000014708	-0.0000007223	-0.0000021700
Z22	0	0	0
Z23	0	0	0
Z24	-0.0000007616	0.0000055418	-0.0000010724
Z25	-0.0000000722	0.0000014733	-0.0000101124
Z26	0	0	0
Z27	-0.0000019708	0	0
Z28	-0.0000020352	0	0
Z29	0	0	0
Z30	0	0	0
Z31	0.0000008731	0	0
Z32	0.0000001185	0	0
Z33	0	0	0
Z34	0	0	0
Z35	-0.0000003232	0	0
Z36	0.0000001153	0	0
Z37	0.0000001151	0	0



**Table 7. The FRINGE Zernike coefficients for the tertiary mirror representing departure from base sphere for each diffraction-limited design.**

	TMCA 96.9 L	TMCF Frozen-Geometry 72.5 L	TMCF Volume-Optimized 59.1 L
Maximum Aperture Semi-Diameter (mm)			
	130.8382	112.8335	95.8424
Normalization Aperture Semi-Diameter (mm)			
	127.0619	112.8335	95.8424
FRINGE Zernike Coefficient, Tertiary Mirror (mm)			
Z1	−0.0000295027	−0.0238951186	−0.0038304336
Z2	0	0	0
Z3	0.0184948453	0.0296065412	0.0334096363
Z4	0.0000075512	−0.0359900827	−0.0057675680
Z5	0.0052708109	0.1735489688	0.1215498815
Z6	0	0	0
Z7	0	0	0
Z8	0.0093525473	0.0148120812	0.0167007000
Z9	−0.0030420183	−0.0121925764	−0.0019534687
Z10	0	0	0
Z11	0.0000009640	−0.0176368745	−0.0117847907
Z12	0.0000197513	0.0014581633	0.0007988727
Z13	0	0	0
Z14	0	0	0
Z15	0.0000638552	0.0000104340	−0.0000074654
Z16	−0.0000270045	−0.0000971190	−0.0000176261
Z17	0.0000038198	−0.0006640551	−0.0004828835
Z18	0	0	0
Z19	0	0	0
Z20	0.0000039500	−0.0001134695	−0.0000401195
Z21	−0.0000051920	0.0000000153	−0.0000066702
Z22	0	0	0
Z23	0	0	0
Z24	−0.0000049411	0.0000034202	−0.0000035400
Z25	0.0000008578	0.0000004933	−0.0000012918
Z26	0	0	0
Z27	−0.0000003919	0	0
Z28	0.0000026877	0	0
Z29	0	0	0
Z30	0	0	0
Z31	0.0000026547	0	0
Z32	−0.0000027713	0	0
Z33	0	0	0
Z34	0	0	0
Z35	−0.0000016328	0	0
Z36	−0.0000014470	0	0
Z37	−0.0000013066	0	0

## Funding

National Science Foundation I/UCRC Center for Freeform Optics (IIP-1338877, IIP-1338898, IIP-1822049 and IIP-1822026) and the National Nuclear Security Administration (DE-NA0001944) through the Frank J. Horton Graduate Research Fellowship awarded by the Laboratory for Laser Energetics at the University of Rochester.

## References

1. J. Reimers, A. Bauer, K. P. Thompson, and J. P. Rolland, "Freeform spectrometer enabling increased compactness," *Light Sci. Appl.* **6**(7), e17026 (2017).
2. A. Bauer, E. M. Schiesser, and J. P. Rolland, "Starting geometry creation and design method for freeform optics," *Nat. Commun.* **9**(1), 1756 (2018).
3. K. Fuerschbach, G. E. Davis, K. P. Thompson, and J. P. Rolland, "Assembly of a freeform off-axis optical system employing three  $\phi$ -polynomial Zernike mirrors," *Opt. Lett.* **39**(10), 2896–2899 (2014).

4. R. Geyl, H. Leplan, and E. Ruch, "Advanced space optics development in freeform optics design, ceramic polishing, rapid and extreme freeform polishing," *Proc. SPIE* **10562**, 105623S (2017).
5. W. B. Wetherell and D. A. Womble, "All-reflective three element objective," U.S. patent US4240707A (December 23, 1980).
6. L. G. Cook, "Reflective optical triplet having a real entrance pupil," U.S. patent US4733955A (March 29, 1988).
7. J. M. Rodgers, "Unobscured mirror designs," *Proc. SPIE* **4832**, 33–60 (2002).
8. E. Muslimov, E. Hugot, W. Jahn, S. Vives, M. Ferrari, B. Chambion, D. Henry, and C. Gaschet, "Combining freeform optics and curved detectors for wide field imaging: a polynomial approach over squared aperture," *Opt. Express* **25**(13), 14598–14610 (2017).
9. J. Zhu, W. Hou, X. Zhang, and G. Jin, "Design of a low F-number freeform off-axis three-mirror system with rectangular field-of-view," *J. Opt.* **17**(1), 015605 (2015).
10. A. Brömel, H. Gross, D. Ochse, U. Lippmann, C. Ma, Y. Zhong, and M. Oleszko, "Performance comparison of polynomial representations for optimizing optical freeform systems," *Proc. SPIE* **9626**, 96260W (2015).
11. "Appendix A Zernike Polynomials," in *CODE V Lens System Setup Reference Manual* (Synopsys Inc., 2018), p. 573.
12. K. Fuerschbach, J. P. Rolland, and K. P. Thompson, "Theory of aberration fields for general optical systems with freeform surfaces," *Opt. Express* **22**(22), 26585–26606 (2014).
13. N. Takaki, A. Bauer, and J. P. Rolland, "On-the-fly surface manufacturability constraints for freeform optical design enabled by orthogonal polynomials," *Opt. Express* **27**(5), 6129–6146 (2019).
14. Z. Zheng, X. Sun, X. Liu, and P. Gu, "Design of reflective projection lens with Zernike polynomials surfaces," *Displays* **29**(4), 412–417 (2008).
15. K. Fuerschbach, "Freeform optical surfaces for field biased and decentered aperture reflective optical design," in *Optical Design and Fabrication 2019 (Freeform, OFT)*, 2019.
16. K. Fuerschbach, J. P. Rolland, and K. P. Thompson, "A new family of optical systems employing  $\phi$ -polynomial surfaces," *Opt. Express* **19**(22), 21919–21928 (2011).
17. A. Rakich and N. Rumsey, "Method for deriving the complete solution set for three-mirror anastigmatic telescopes with two spherical mirrors," *J. Opt. Soc. Am. A* **19**(7), 1398–1405 (2002).
18. A. Rakich, "Reflecting anastigmatic optical systems: a retrospective," *Opt. Eng.* **57**(10), 101701 (2018).
19. D. Korsch, "Closed-form solutions for imaging systems, corrected for third-order aberrations," *JOSA* **63**(6), 667–672 (1973).
20. J. R. Rogers, "Techniques and tools for obtaining symmetrical performance from tilted-component systems," *Opt. Eng.* **39**(7), 1776–1787 (2000).
21. R. A. Buchroeder, "Tilted-component telescopes. Part I: theory," *Appl. Opt.* **9**(9), 2169–2171 (1970).
22. R. A. Buchroeder, "Design Examples of Tilted-Component Telescopes (TCT's) (A Class of Unobscured Reflectors)," in *Optical Sciences Technical Report*, No. 68 (Optical Sciences Center, University of Arizona, 1971).
23. R. A. Buchroeder, "Tilted component optical systems," PhD, University of Arizona (1976).
24. J. C. Papa, J. M. Howard, and J. P. Rolland, "Starting point designs for freeform four-mirror systems," *Opt. Eng.* **57**(10), 101705 (2018).
25. G. W. Forbes, "Robust, efficient computational methods for axially symmetric optical aspheres," *Opt. Express* **18**(19), 19700–19712 (2010).
26. "Chapter 3 Optimization Modes," in *CODE V Optimization Reference Manual*, Version 11.2 (Synopsys Inc.) (2018).